RSC Advances

PAPER

View Article Online
View Journal | View Issue

Check for updates

Cite this: *RSC Adv.*, 2024, **14**, 3232

Epitaxial graphene growth on cubic silicon carbide on silicon with high temperature neutron reflectometry: an *operando* study†

Aiswarya Pradeepkumar, [ab] David Cortie, [cd] Erin Smyth, [c] Anton P. Le Brun [c] and Francesca Iacopi *[abd]

The growth of graphene on silicon carbide on silicon offers a very attractive route towards novel wafer-scale photonic and electronic devices that are easy to fabricate and can be integrated in silicon manufacturing. Using a Ni/Cu catalyst for the epitaxial growth of graphene has been successful in the mitigation of the very defective nature of the underlying silicon carbide on silicon, leading to a consistent graphene coverage over large scales. A more detailed understanding of this growth mechanism is warranted in order to further optimise the catalyst composition, preferably *via* the use of *operando* characterization measurements. Here, we report *in situ* neutron reflectometry measurements of (Ni, Cu)/SiC films on silicon wafers, annealed from room temperature to 1100 °C, which initiates graphene formation at the buried (Ni, Cu)/SiC interface. Detailed modelling of the high temperature neutron reflectometry and corresponding scattering length density profiles yield insights into the distinct physical mechanisms within the different temperature regimes. The initially smooth solid metallic layers undergo intermixing and roughening transitions at relatively low temperatures below 500 °C, and then metal silicides begin to form above 600 °C from interfacial reactions with the SiC, releasing atomic carbon. At the highest temperature range of 600–1100 °C, the low neutron scattering length density at high temperature is consistent with a silicon-rich, liquid surface phase corresponding to molten nickel silicides and copper. This liquid catalyst layer promotes the liquid-phase epitaxial growth of a graphene layer by precipitating the excess carbon available at the SiC/metal interface.

Received 5th December 2023
Accepted 13th January 2024

DOI: 10.1039/d3ra08289j

rsc.li/rsc-advances

Open Access Article. Published on 19 2024. Downloaded on 11.05.26 11:41:40.
This article is licensed under a Creative Commons Attribution-NonCommercial 3.0 Unported Licence.

1 Introduction

Epitaxial graphene (EG) on cubic silicon carbide (3C–SiC) on silicon substrates could enable tunable electronic, optoelectronic and photonic devices integrated with well-established silicon technologies. A promising avenue is to grow relatively thick SiC films (~500 nanometres) on silicon, which act as "pseudosubstrates" for graphene growth. While the growth of epitaxial graphene on 4H– and 6H–SiC wafers has reached a peak of maturity,[1–6] the corresponding growth on 3C–SiC on silicon pseudosubstrates has been plagued by many more challenges related to the poor heteroepitaxial SiC template[7] and also to the unstable SiC/silicon interface.[8,9] As the issues of the electrically "leaky" SiC/silicon interface have been better understood and addressed,[10,11] the attention has been focused on an improved understanding and control of the catalytic Ni/Cu approach to grow epitaxial graphene on SiC/silicon.[12–14] This method enables the realisation of a consistent large-scale and site-selective epitaxial growth,[15,16] yielding a conductivity as high as that of EG on SiC wafers, despite considerably smaller grain sizes.[14]

We have reported that the use of a Ni/Cu bilayer on the 3C–SiC[12,14] enables uniform graphene growth over large scales despite the highly defective 3C–SiC as opposed to the conventional thermal decomposition route of 3C–SiC.[17] The catalytic reaction of nickel with SiC forming nickel silicides and releasing atomic carbon, combined with that of the copper distributing the released carbon across large areas and promoting its graphitisation, enable a continuous graphene coverage in spite of the highly defective nature of the heteroepitaxial 3C–SiC surface.[12] Particularly, we had attributed this improvement to the liquid-phase epitaxial growth[18–20] conditions of this system at 1100 °C, providing the carbon atoms with longer diffusion lengths as compared to the more conventional solid-phase epitaxy *via* thermal decomposition of 3C–SiC.[12]

[a]*School of Electrical and Data Engineering, Faculty of Engineering and Information Technology, University of Technology Sydney, Sydney, New South Wales, 2007, Australia. E-mail: Francesca.Iacopi@uts.edu.au*

[b]*ARC Centre of Excellence for Transformative Meta-Optical Systems, University of Technology Sydney, New South Wales, 2007, Australia*

[c]*Australian Centre for Neutron Scattering, Australian Nuclear Science and Technology Organization, New Illawarra Road, Lucas Heights, New South Wales 2234, Australia. E-mail: dcr@ansto.gov.au*

[d]*ARC Centre of Excellence in Future Low-Energy Electronics Technologies, Melbourne, Victoria, 3800, Australia*

† Electronic supplementary information (ESI) available. See DOI: https://doi.org/10.1039/d3ra08289j

© 2024 The Author(s). Published by the Royal Society of Chemistry

Open Access Article. Published on 19 2024. Downloaded on 11.05.26 11:41:40.
This article is licensed under a Creative Commons Attribution-NonCommercial 3.0 Unported Licence.

Operando techniques can facilitate new insights and a thorough corroboration of this epitaxial growth mechanism, enabling future advancements in terms of grain size and layer control of this EG process. In this work, we performed an *in situ* growth of EG on 3C–SiC/Si and investigated the temperature dependence of the alloy-mediated graphene layer formation by probing light elements using time-of-flight neutron reflectometry.

Neutron reflectometry is a surface-sensitive form of neutron scattering that can probe the chemical depth-profiles of films in the 0.5–300 nm thickness range, and yield information on buried interfaces below the surface. In addition, it can provide *operando* measurements, thanks to the low rate of interaction of neutrons with matter.

Specular neutron and X-ray reflectometry has been performed in the past on thick many-layer (15–100 layers) graphene grown on the C-face of 4H–SiC substrates.[6] These measurements revealed the important role of disorder and roughness on the SiC/graphene growth interface. Off-specular measurements also demonstrated the existence of a distinctive type of diffuse scattering known as "Yoneda" scattering giving characteristic "angel wings" in off-specular reflectometry, evident in transverse scans that probe in-plane directions, tied to the existence of moderate nanometre-scale roughness at the SiC/C interface with a distinct lateral correlation length. The latter specular and off-specular data provide a useful point of comparison, however the earlier measurements, were only performed post-annealing, and to-date there have been no high temperature neutron reflectometry which would allow for an *operando* study of the growth mechanisms in detail at different temperature stages. Furthermore, the low-temperature growth of carbon on 3C–SiC pseudo substrates, mediated by Ni and Cu layers, is considerably different from the growth on monocrystalline 4H–SiC wafers, as the catalytic interactions with metallic films from silicide formation play a key role in lowering the reaction temperature.

2 Experimental

2.1 Epitaxial graphene synthesis

We have used unintentionally doped, commercially-purchased (NovaSiC, France) 3C–SiC(100) films with 500 nm thickness, epitaxially grown on 700 μm thick highly resistive (resistivity >10 kΩ cm) Si(100) substrates. Prior to graphene growth, the 3C–SiC/Si substrate wafers are diced into 2×2 cm^2 coupons and cleaned in acetone and isopropanol. The EG is obtained *via* a solid-source, Ni/Cu alloy-mediated method as described by Mishra *et al.*[12] The steps involved in the EG synthesis process are as follows: (i) Ni and Cu are deposited *via* sputtering on the top of the SiC surface as separate layers with thicknesses of 10 nm and 20 nm, respectively (see Fig. 1); (ii) samples are annealed at 1100 °C below 5×10^{-5} mbar for 1 hour; (iii) samples are wet etched in a freckle etch solution[12] (~16 hours) to remove the residues of metal and metal-silicides, followed by rinsing in Milli-Q water.

2.2 Neutron reflectometry

In this work, we performed an *in situ* growth of EG on the 3C–SiC(100)/Si(100) and investigated the temperature-dependence of the alloy-mediated graphene layer formation using neutron reflectometry (NR). Variable temperature neutron reflectometry measurements were conducted *in situ* during a controlled annealing process on the Spatz time-of-flight neutron

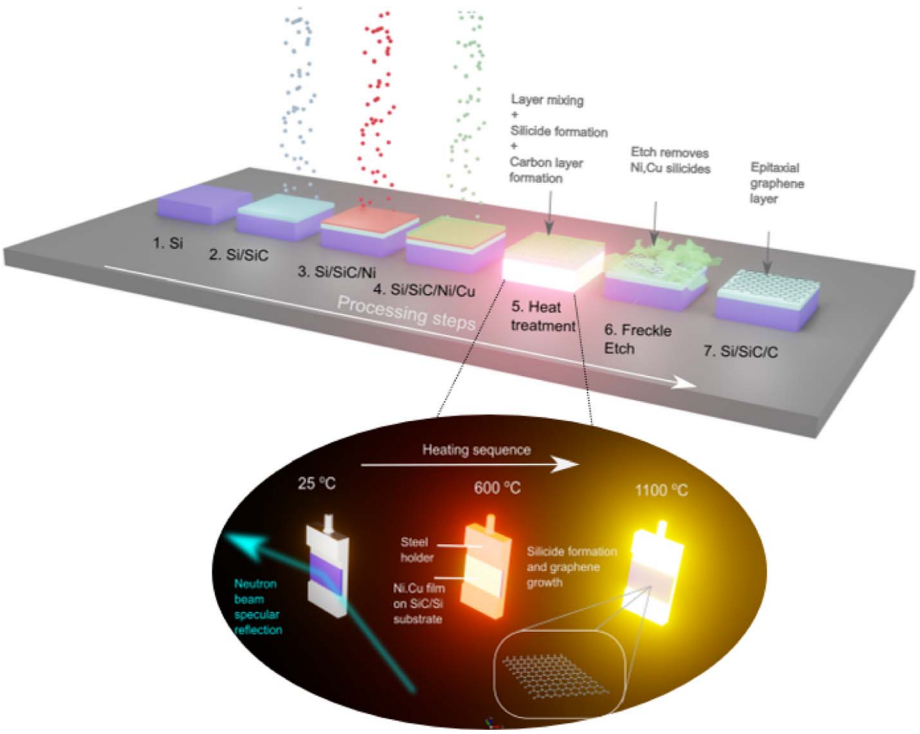

Fig. 1 Schematic of the Ni/Cu catalytic alloy-mediated EG synthesis on 3C–SiC on silicon.

Open Access Article. Published on 19 2024. Downloaded on 11.05.26 11:41:40.
This article is licensed under a Creative Commons Attribution-NonCommercial 3.0 Unported Licence.

reflectometer at the 20 MW OPAL Multipurpose Reactor at the Australian Nuclear Science and Technology Organisation (ANSTO, Lucas Heights, Australia). The advantage of using neutrons for this application is that the neutron beam can penetrate through a vacuum furnace walls containing elements of niobium and aluminium to observe the conditions for graphene growth at 1100 °C. These types of measurements would be impossible with standard X-ray reflectometry (XRR) as X-rays cannot penetrate through the furnace's outer and inner walls. In addition, neutrons are advantageous for observing and differentiating lighter elements with similar mass such as carbon, oxygen and silicon, all involved in the graphene synthesis. This is related to their larger and distinct neutron scattering lengths.[19] In contrast, X-ray scattering lengths for carbon, oxygen and silicon are relatively smaller and similar, making these elements less sensitive under X-rays, especially when higher atomic number elements like Ni and Cu are also present.[22] Furthermore, neutrons also exhibit better contrast for Ni and Cu, whereas they are less distinct under X-rays.[22]

Spatz is a time-of-flight reflectometer using cold neutrons with wavelengths from 2–20 Å, in a vertical scattering geometry as shown in Fig. 2.[21] The data was reduced using the RefNX software package, and plotted in terms of the reduced scattering vector:

$$Q_z = 4\pi \frac{\sin(\Theta)}{\lambda}$$

where Θ is the scattering angle, and λ is the neutron wavelength. The specular reflectometry data were fitted using the RefNX software.[23] In the data fitting the system is divided into a series of layers and each layer is defined by its thickness (in Å), its scattering length density (SLD, in $\times 10^{-6}$ Å^{-2}), and roughness (in Å). Each parameter in each layer is varied within physically relevant limits along with background using a differential evolution algorithm until the fitted data matches the experimental data with a minimized χ^2 value. Once a good fit with the differential evolution algorithm is achieved the fits were repeated using a Markov chain Monte Carlo (MCMC)[24] routine using 2000 steps, 200 walkers, and a thinning of 1 yielding a total of 2000 fits. This results in a spread of possible fits[12] and the reported values are the median values for each variable parameter from this spread and the error is the standard deviation.

2.2.1 ***In situ*** **high temperature treatment.** A high temperature vacuum furnace (maximum temperature 1600 °C) was mounted at the sample position on Spatz as shown in Fig. 2b. The furnace was designed by the Institut Laue-Langevin (ILL), where the heat is generated by passing a 300 A current through a thin cylindrical niobium element that contains the sample volume in the core. Eight layers of thin niobium radiation shields are used to maintain a uniform temperature at the sample shielding, and for radiation shielding. The outer furnace body is made of aluminum which is highly transparent to neutrons. The neutron transmission through the furnace exceeded 85% over the usable wavelength range 2–20 Å on Spatz. All reflectometry measurements were reduced using direct beam measurements through the furnace itself. A turbomolecular pump is used to pump the sample volume achieving base pressures in the range from 10^{-7} to 10^{-6} mbar. The sample was mounted on a vertical probe stick, on a stainless-steel (grade 304 holder) capable of withstanding high temperatures.

2.3 X-ray reflectometry

Specular and off-specular X-ray reflectometry were performed using a Rigaku Smartlab II diffractometer where the X-ray wavelength was 1.5406 Å (Cu K-α). Specular data were fitted using the RefNX software. Modelling of the off-specular data used the BornAgain software[25] deploying the Distorted Wave Born Approximation to model the Yoneda wings and correlated roughness.

2.4 Raman spectroscopy

Room temperature (RT) Confocal Raman mapping was performed using a Renishaw InVia Raman spectrometer at 532 nm

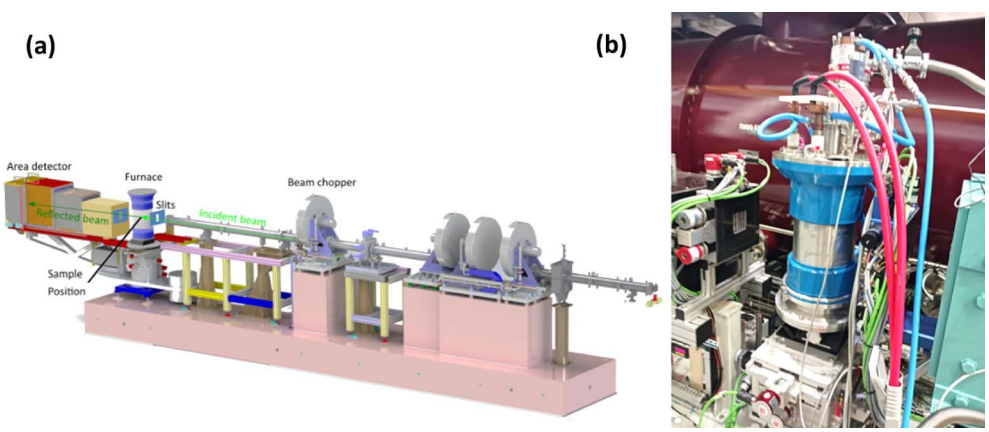

Fig. 2 (a) The layout of the Spatz neutron beam instrument with furnace installed on the neutron beamline at the Australian Nuclear Science and Technology Organization (ANSTO), recreated from ref. 21 under creative commons licence CC BY 4.0 DEED. Green arrow indicates the neutron beam path. (b) Photograph of the furnace installed on the neutron beamline for EG synthesis and *in situ* monitoring using neutron reflectometry at ANSTO.

© 2024 The Author(s). Published by the Royal Society of Chemistry

Open Access Article. Published on 19 2024. Downloaded on 11.05.26 11:41:40.
This article is licensed under a Creative Commons Attribution-NonCommercial 3.0 Unported Licence.

laser using a 100× objective with a spot size of ~1 μm and incident power of 17 mW.[12] Raman mapping was performed across an area of 30 μm × 30 μm at the center of the samples using a 0.2 μm step size and 0.1 s integration time. Raman intensity ratio maps of the D to G peak (I_D/I_G) and 2D to G peak (I_{2D}/I_G) are analyzed.

2.5 Electrical characterization

Four-point InSn were soldered onto the EG/3C–SiC(100)/Si(100) annealed sample after wet freckle etching. Room temperature van-der Pauw Hall effect measurements were performed to measure the carrier type, carrier concentration, mobility and sheet resistance across a current range of 1–10 μA using an Ecopia Hall effect measurement system, HMS 5300 operating with a magnetic field of 0.55 T.

3 Results and discussions

3.1 High temperature *in operando* neutron reflectometry

Fig. 3 shows the neutron reflectivity *versus* scattering vector, Q for different annealing temperatures starting from room temperature (RT) to 600 °C for the Cu/Ni/3C–SiC(100)/Si(100). The solid points are the data, and the solid lines are the corresponding fitting curves. Kiessig fringes are observed in Fig. 3 for the lower temperature data (<400 °C), which are related to the Ni and Cu layers with different SLDs. A slab model was used to fit the data with the top layer of Cu of thickness of 214.2 (±26.6) Å, SLD of 6.2 (±0.1) × 10^{-6} Å^{-2} and roughness of 11.8 (±5.0) Å, (see ESI Table S1† for fitted parameters).

The Cu layer is followed by the Ni layer of thickness, SLD and roughness of 85.3 (±1.2) Å, 7.0 (±0.1) × 10^{-6} Å^{-2} and 1.6 (±2.2) Å, respectively. Whilst the copper layer matches expectation, the SLD value of the nickel layer is reduced by 15% from the value expected for fully dense nickel (mass density 7.9 g cm^{-3}, SLD = 8.35 × 10^{-6} Å^{-2}). This may reflect the nanocrystalline nature of the nickel layer which typically reduces the mass density by 10–20%, although some low-temperature interdiffusion with the copper may also contribute. The fitted SLD of the SiC substrate is 5.2 (±0.1) × 10^{-6} Å^{-2}, matching the expected SLD based on the 3C crystal structure. The SiC has a roughness of 2.0 Å, determined in the neutron measurements. The SiC pseudo-substrate is sufficiently thick (~500 nm) so that it appears as semi-infinite to the neutrons, and the underlying silicon layer is not detected, as the latter would yield an SLD of 2.01 × 10^{-6} Å^{-2} which is not detected experimentally. As temperature increases to 400 °C, the well-defined maxima and minima of the fringes gradually dampen, indicating the intermix of Ni and Cu layers and Ni–Cu alloy formation. The Kiessig fringes disappear at 600 °C. This is attributed to a sudden increase in surface/interface roughness, and also a loss of neutron scattering length density contrast as the surface layer SLD is decreased. Both phenomena indicate the start of a solid phase reaction, implying the onset of nickel silicides formation ($NiSi_2$ in this case, as indicated in ref. 12), leading to silicon entering the surface region and reducing the SLD. This in turn implies the release of atomic carbon. The formation of $NiSi_2$ at 600 °C is in good agreement with earlier reports in literature.[26,27] Fig. 4 shows the corresponding SLD profiles *versus* distance for the fitted models from Fig. 3. The SLD profiles calculated for RT and 200 °C indicate the two distinct layers of Ni and Cu deposited on top of 3C–SiC for the EG synthesis. The data at 400 °C shows the alloy formation of Ni and Cu. Fig. 4 indicates that at 600 °C, the cupronickel layer and top SiC layers intermix to form nickel $NiSi_2$. The 600 °C data indicates indeed a very diffuse, graded interface attributed to a diffusion profile of the silicon, copper and nickel related to a complex elemental concentration across the sample.

After 1 hour of annealing at 1100 °C, data in Fig. 5 indicate the formation of a low-density surface layer with an SLD of 2.6 (±1.2) × 10^{-6} Å^{-2} (refer to Supplementary Table S2† for fitted values). This low-density layer can be related to the formation of a molten top layer at 1100 °C made of liquid nickel silicides/copper (melting points of $NiSi_2$ and Cu are ~993 °C and ~1085 °C, respectively), supporting a liquid-phase epitaxial growth of EG.[12,13] This growth condition can hence greatly

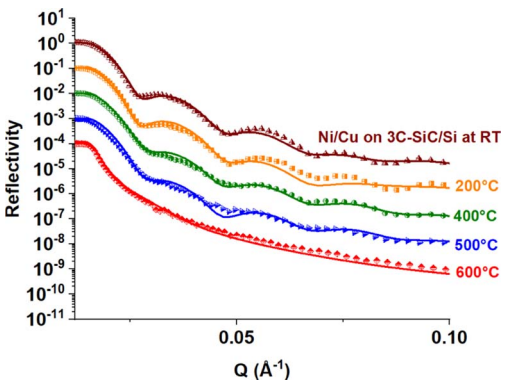

Fig. 3 Neutron reflectivity experimental data obtained during the *in situ* annealing from room temperature to 600 °C of the thin Ni/Cu bilayer sputtered on 3C–SiC(100)/Si(100) for the growth of epitaxial graphene. Data are offset for clarity. Solid points represent the experimental data and solid lines represent the fitted curves.

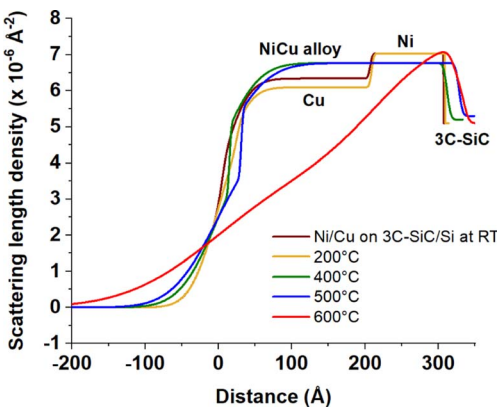

Fig. 4 Calculated real-space SLD profiles corresponding to the data in Fig. 3. Note the Ni/Cu bilayer alloying above 200 °C and the high intermixing of the cupronickel alloy and the top of the SiC layer, indicating the start of formation of $NiSi_2$, at 600 °C.

Open Access Article. Published on 19 2024. Downloaded on 11.05.26 11:41:40.
This article is licensed under a Creative Commons Attribution-NonCommercial 3.0 Unported Licence.

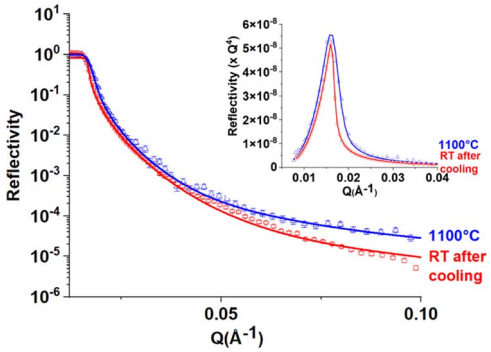

Fig. 5 Neutron reflectivity experimental and fitted data obtained at 1100 °C and after the sample returned to RT – Markov chain Monte Carlo (MCMC) sampling data is shown in the supplementary. Dots represent the experimental data and solid lines represent the fit. The inset shows the reflectivity data and fit on the RQ^4 scale for reflectivity over a limited Q range to highlight the differences between the two datasets.

benefit from a liquid-assisted diffusion[18–20] during the carbon epitaxy. The data is fitted with a layer of carbon underneath the molten layer (see, Fig. 6) with thickness, SLD and roughness of 13.1 (±6.0) Å, 6.8 (±3.3) × 10^{-6} $Å^{-2}$ and 7.7 (±5.3) Å respectively, indicating the graphene formation. Additionally, the data at 1100 °C could only be fitted with a silicate (Si–O–C) layer between the EG and the SiC, with thickness, SLD and roughness of 9.3 (±6.2) Å, 4.5 (±1.7) × 10^{-6} $Å^{-2}$ and 5.2 (±3.1) Å, respectively (Supplementary Table S2†). This agrees with cross-sectional transmission electron microscopy (TEM) and time of flight secondary ion mass spectrometry (ToF-SIMS) depth profiling of graphene samples we reported in ref. 12, indicating the presence of graphene layer on top of a low-density silicate layer on the 3C–SiC.

The final RT measurement after cooling down shows a reduction of the thickness of the top-intermixed catalytic layer to 10.9 (±5.6) Å, from 34.0 (±24.2) Å at 1100 °C indicating a loss of metal by evaporation (primarily Cu, due to its appreciable volatility already from ~400 °C[28]) during the high-temperature annealing. The loss of metallic elements during annealing is also evident from the decrease in total thickness of the metallic layers on top of the SiC from ~300 (±27.8) Å before annealing to ~10.9 (±5.6) Å after cooling back to RT, as shown in Table S1 and S2.† The RT data after cooling down, show the presence of a carbon (graphene) layer peak below the top/catalytic layer. The carbon layer representing the graphene was fitted with an SLD and roughness of 6.5 (±1.7) × 10^{-6} $Å^{-2}$ and 10 (±4.8) Å, respectively. The silicate layer between the graphene and SiC was fitted with a thickness, SLD and roughness of 17.9 (±3.9) Å, 3.2 (±0.2) × 10^{-6} $Å^{-2}$ and 1.3 (±1.8) Å, respectively.

MCMC sampling data for 1100 °C and RT is shown in the ESI Fig. S1–S2.† Although there is a large spread of fitted values for the graphene layer, this is to be expected given the featureless nature of the experimental data. However, note that it was not possible to fit the data adequately without adding the carbon (EG) and silicate layers. Additionally, as the thicknesses are comparable or smaller than layer roughness in several case, due to the diffuse and complex depth profile, the validity of the standard specular reflectometry calculation needs to be confirmed. In the ESI Fig. S3,† we present alternate calculations using micro-slicing of the SLD profile.

3.2 Ex-situ characterization

After the annealing step and *in situ* neutron measurements discussed earlier, the same samples were removed from the furnace and studied under ambient condition using X-ray and neutron reflectometry. Additional samples prepared on a standard laboratory furnace were also measured for comparison.

3.2.1 X-ray reflectometry. Initially the sample was studied with the Ni/Cu on 3C–SiC/Si before annealing. The X-ray reflectivity patterns in Fig. 7 demonstrate clear differences for the (Ni, Cu)/SiC film before and after annealing. These include the loss of Kiessig fringes and the rapid-falloff in the *Q*-dependent intensity of reflectivity for samples after the heat treatment process. This is consistent with the reaction and roughening of the Ni, Cu layer, and some loss of the metallic elements at high temperature. Fig. 8 shows the X-ray SLD profile for the (Ni, Cu)/SiC film before and after heating. The X-ray SLD for Ni and Cu are similar, so these are not identified as separate layers in the

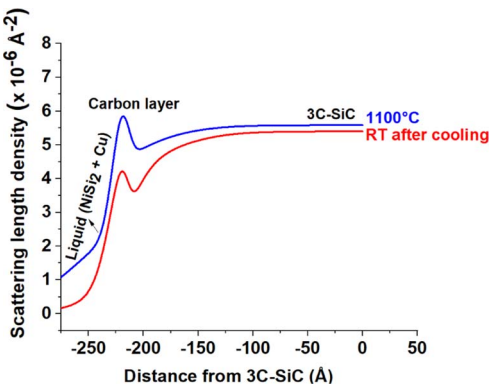

Fig. 6 SLD profiles for the fitted models for data at 1100C and after cooling to room temperature. MCMC sampling data is shown in the ESI, Fig. S1–S2.†

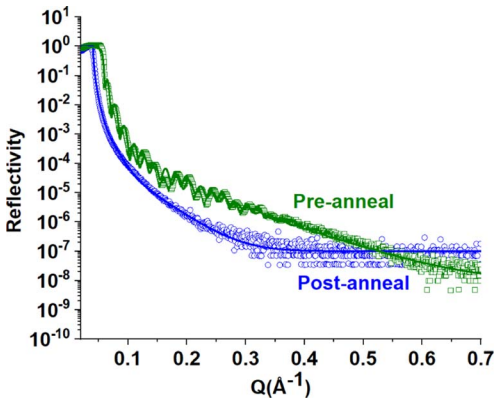

Fig. 7 X-ray reflectivity of Ni/Cu sputtered 3C–SiC(100)/Si substrate before and after annealing, prior to etching. Solid lines indicate the fit.

© 2024 The Author(s). Published by the Royal Society of Chemistry

Open Access Article. Published on 19 2024. Downloaded on 11.05.26 11:41:40.
This article is licensed under a Creative Commons Attribution-NonCommercial 3.0 Unported Licence.

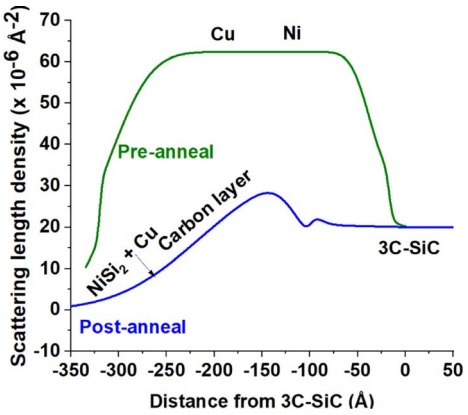

Fig. 8 SLD profiles for the fitted models for Ni/Cu sputtered 3C–SiC(100)/Si substrate before and after annealing, prior to etching.

pre-annealed data. As the X-ray SLD for Si and C are similar, the carbon rich layers do not appear as a peak in the post-annealed X-ray SLD, however it is clear the surface of the SiC has been dramatically modified, and in particular the effective roughness. This causes the reflectivity intensity to fall off more rapidly with the scattering vector in the post-annealed sample compared to the pre-annealed Ni/Cu sputtered 3C–SiC/Si samples.

In addition to the samples used for neutron measurements, X-ray reflectometry measurements were performed on an EG film grown in a standard Carbolite laboratory HT furnace used in ref. 14-see Fig. 9. Fig. 9a shows that the specular reflectivity of final epitaxial graphene (post-heating and etching) is different from the bare 3C–SiC/Si. These measurements can also be compared closely with the structural data for similar films in ref. 12 and reflectometry studies of graphene on 4H–SiC in ref. 6. The reflectivity intensity falls off more rapidly with the scattering vector (Q) in the EG samples compared to the 3C–SiC/Si samples. This implies that the surface roughness of graphene is larger than 3C–SiC/Si. We have previously reported that the root mean square roughness of alloy-mediated epitaxial graphene is about two-fold (~9 nm) of the 3C–SiC/Si roughness (4 nm) as determined by atomic force microscopy.[12] The X-ray and neutron roughness, which are both probes of the global average across the entire sample, are somewhat smaller, however display the same relative trend. There is also some indication of a single weak Kiessig fringe at $-Q = 0.1$ Å^{-1} in the EG samples, however it is heavily damped. Pristine, idealised graphene should yield well resolved fringes, albeit at higher Q. Previous work explained the observation of the damped fringe in SiC/EG as a result of the interlayer that forms between the graphene and SiC during the growth process.[6] Here a simple two-layer model was used to fit the data as represented by the SLD profiles in Fig. 9b. The EG sample shows an additional thin layer. This is consistent with past reports[6] (for example see, Fig. 5 of ref. 6) where it is attributed to a rough interface layer that forms between the EG and the SiC.

Through an off-specular XRR, we observed distinctive Yoneda scattering in the off-specular map, again implying that the surfaces of the films were rough, see Fig. 10. This yields a distinctive 3-peak rocking curve in the transverse scans. The observation of Yoneda scattering in SiC:C interfaces was reported previously in ref. 6 and the diffuse and off-specular scattering in our samples is remarkably similar. The origin of the scattering was proposed to arise from the SiC rough interface formed during the growth, however, has not been analysed quantitatively. To analyse the source of the scattering, calculations were performed in the Distorted Wave Born Approximation (DWBA). The model used a 29 Å roughness, and this roughness is primarily on the SiC surface, with a Hirst-factor of 0.1 and correlation length set to 3300 Å. The distinctive 2D map yields information on the correlation lengths in the bare SiC and EG coated SiC thin films. In particular, from the critical angle of the Yoneda scattering it is clear that the primary rough interface is at the SiC interface. If the graphene were thick enough or rough enough a second set of Yoneda wings should be observed. This finding confirmed by control measurements that revealed even blank SiC pseudosubstrate (even those without EG) yielded weak Yoneda scattering indicating the films are intrinsically rough. However, the nature of the 2D scattering was modified by the annealing process and EG formation, indicating additional roughness and disorder at EG/SiC

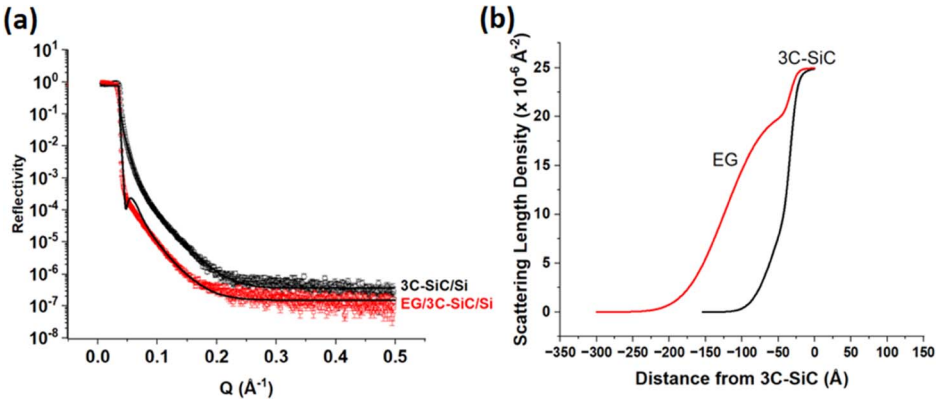

Fig. 9 (a) X-ray reflectivity of bare 3C–SiC(100)/Si(100) substrate and EG/3C–SiC(100) after freckle etching produced ex-situ (non-neutron). (b) SLD profile for the fitted model. The reflectivity intensity falls off more rapidly in the EG samples. This implies that the surface roughness of graphene is larger than 3C–SiC/Si.

Open Access Article. Published on 19 2024. Downloaded on 11.05.26 11:41:40.
This article is licensed under a Creative Commons Attribution-NonCommercial 3.0 Unported Licence.

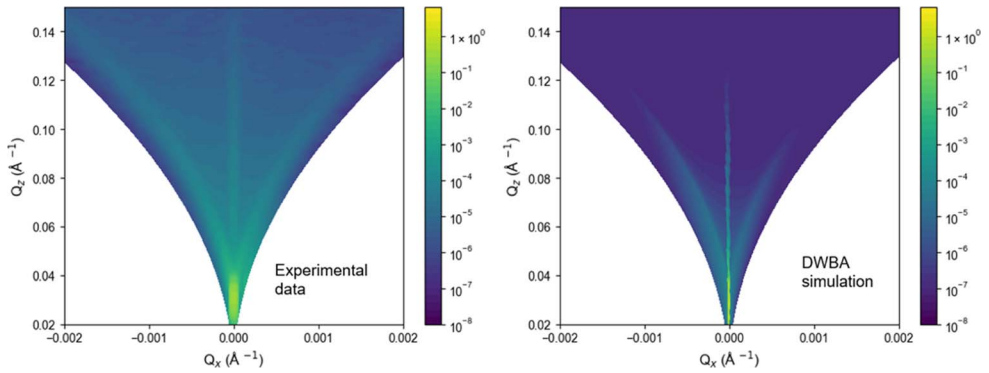

Fig. 10 Off-specular X-ray reflectometry pattern of the SiC:C interface showing the distinctive Yoneda "angel" wing scattering leading to the "V" shaped intensity around the primary specular peak which is vertical at ($Q_x = 0$).

interface. It is noted the Yoneda-wing patterns are comparable with the previous data for single crystal SiC:C interfaces[6] suggesting that the alloy-mediated approach yields samples with comparable quality to the graphene obtained at higher temperature on monocrystalline SiC substrates.

3.2.2 Neutron reflectometry – after wet-freckle etch. Fig. 11 shows the neutron reflectivity data for the annealed sample after it has undergone a wet freckle etching to remove the top silicate layer. The data was fitted with a carbon layer on top indicating the graphene layer with thickness and roughness ranges of 3.0–8.0 Å, and 8.0–12.0 Å, respectively. The final fit showed a graphene layer with an average SLD of 4×10^{-6} Å^{-2}. This is smaller than the value estimated for a mono/bi-layer graphene on 4H–SiC(0001), which is 7.5×10^{-6} Å^{-2} (estimated from a density of 2.267 g cm^{-3} given in ref. 29) and suggests that the mass density is lower in our case. We relate the lower mass density to the turbostratic nature of the graphene synthesized by alloy-mediated approach adopted in this work.[14] Turbostratic graphene is reported to have a lower mass density[30] of 1.12 g cm^{-3}, resulting in an SLD of 3.7×10^{-6} Å^{-2} similar to what we observed. The SiC was fitted with an SLD of 5.0×10^{-6} Å^{-2} and a roughness of 50 Å. A silicate or Si–O–C layer was fitted with a thickness of 19.7 ($\pm$1.6) Å and SLD of 2.7 ($\pm$0.1) $\times 10^{-6}$ Å^{-2}. The corresponding SLD profile for the data is shown in Fig. 12, where the top carbon (graphene) layer is evident as a peak, followed by the oxidized layer and the SiC.

3.2.3 Raman spectroscopy. Fig. 13 shows the average Raman spectrum of the sample annealed during the *in situ* neutron study, after the cooling and a wet freckle etching step. The figure indicates the D, G, and 2D Raman bands of graphene. Fig. S4† shows the ratio of intensity maps of the D to G peak (I_D/I_G) and 2D to G peak (I_{2D}/I_G). The maps show only a small variation across the sample indicating the graphene coverage is uniform. A comparison of average Raman maps for graphene sample before and after freckle etching is shown in the supplementary Fig. S5.†

3.2.4 Electrical characterization. We performed room temperature van der Pauw Hall effect characterization of the annealed samples (furnace installed *in situ* on the neutron beamline) after a wet freckle etching. Table S4† shows the room temperature transport properties. The EG synthesized in this work, indicate a p-type conduction with a sheet carrier concentration of 5.5 ($\pm$0.2) $\times 10^{12}$ cm^{-2} mobility of 331 ($\pm$1)

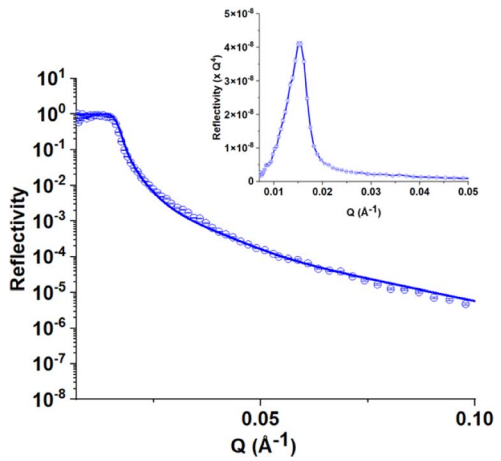

Fig. 11 Neutron reflectivity experimental and fitted data obtained for the annealed sample after wet freckle etching. The inset shows the reflectivity data and fit on the RQ^4 scale for reflectivity over a limited Q range.

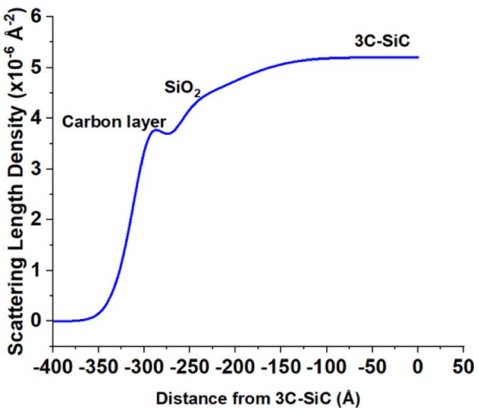

Fig. 12 SLD profiles for the fitted models for data for the annealed sample after wet freckle etching.

© 2024 The Author(s). Published by the Royal Society of Chemistry

Open Access Article. Published on 19 2024. Downloaded on 11.05.26 11:41:40.
This article is licensed under a Creative Commons Attribution-NonCommercial 3.0 Unported Licence.

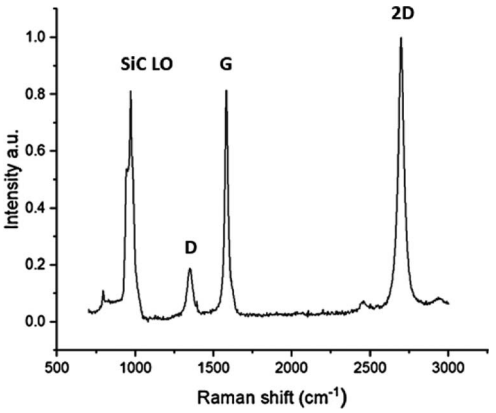

Fig. 13 Raman averaged spectrum across a 30 × 30 μm^2 area on the annealed sample after wet freckle etch.

cm^2 V^{-1} s^{-1} and sheet resistance of 3.4 (±0.2) k Ω^{-1}. The p-type conduction is understood to reflect oxygen doping, which is a feature of the Si–O–C layer that forms underneath the EG during the annealing step.[14]

4 Conclusions

With a unique *in operando* (up to 1100 °C, below 5 × 10^{-5} mbar) neutron reflectometry setup and characterisation, this work gain insights into the epitaxial growth of graphene on 3C–SiC/Si using a thin bilayer of Ni/Cu as catalyst. The observations directly confirm that the metal silicide formation is a key ingredient enabling the release of atomic C from the SiC at relatively low temperatures to enable the formation of graphene. The *operando* observations also support the liquid-phase nature of the epitaxial growth occurring at 1100 °C, key to a uniform coverage of graphene despite of the very defective 3C–SiC template.

Overall, the neutron reflectivity profiles sequentially illustrate all of the main steps and hallmarks of this epitaxial growth;

(a) Alloying of the Ni/Cu bilayer at 400 °C.

(b) Onset of nickel silicidation at 600 °C creating a highly intermixed layer on top of the 3C–SiC.

(c) Formation of a low-density, likely molten, catalyst layer around 1100 °C.

(d) Formation of a carbon (graphene) layer at 1100 °C, underneath the molten catalyst, and a thin silicate (Si–O–C) layer (SLD of 2.7 × 10^{-6} Å^{-2}) in between the graphene and silicon carbide of thickness of ∼20 Å.

This work unlocks new avenues to use high temperature neutron reflectometry for the observation and optimization of wafer-scale growth of epitaxial graphene and other 2D materials for nanoelectronics and photonics.

Author contributions

The manuscript was written through the contributions of all authors.

Conflicts of interest

There are no conflicts to declare.

Acknowledgements

This research was partly supported by an AINSE Ltd. Early Career Researcher Grant (ECRG). This work was performed in part at the Australian Nuclear Science and Technology Organization. We thank ANSTO for providing neutron beamtime *via* proposal (14446). Spatz neutron beam operations are supported through the National Collaborative Research Infrastructure Strategy (NCRIS), an Australian Government initiative. We acknowledge Chris Baldwin and Michael Fenech for technical support at the Australian Centre for Neutron Scattering, ANSTO. AP and FI also acknowledge support by the ARC Centre of Excellence for Transformative Meta-Optical Systems (CE200100010).

References

1 C. Berger, Z. Song, T. Li, X. Li, A. Y. Ogbazghi, R. Feng, Z. Dai, A. N. Marchenkov, E. H. Conrad and P. N. First, Ultrathin epitaxial graphite: 2D electron gas properties and a route toward graphene-based nanoelectronics, *J. Phys. Chem. B*, 2004, **108**, 19912–19916.

2 J. L. Tedesco, B. L. VanMil, R. L. Myers-Ward, J. M. McCrate, S. A. Kitt, P. M. Campbell, G. G. Jernigan, J. C. Culbertson, C. Eddy and D. K. Gaskill, Hall effect mobility of epitaxial graphene grown on silicon carbide, *Appl. Phys. Lett.*, 2009, **95**, 122102.

3 Y.-M. Lin, C. Dimitrakopoulos, K. A. Jenkins, D. B. Farmer, H.-Y. Chiu, A. Grill and P. Avouris, 100-GHz transistors from wafer-scale epitaxial graphene, *Science*, 2010, **327**, 662.

4 F. Speck, J. Jobst, F. Fromm, M. Ostler, D. Waldmann, M. Hundhausen, H. B. Weber and T. Seyller, The quasi-free-standing nature of graphene on H-saturated SiC (0001), *Appl. Phys. Lett.*, 2011, **99**, 122106.

5 W. Norimatsu and M. Kusunoki, Structural features of epitaxial graphene on SiC {0 0 0 1} surfaces, *J. Phys. D: Appl. Phys.*, 2014, **47**, 094017.

6 A. Mazza, A. Miettinen, A. Daykin, X. He, T. Charlton, M. Conrad, S. Guha, Q. Lu, G. Bian and E. Conrad, Revealing interfacial disorder at the growth-front of thick many-layer epitaxial graphene on SiC: a complementary neutron and X-ray scattering investigation, *Nanoscale*, 2019, **11**, 14434–14445.

7 N. Mishra, J. Boeckl, N. Motta and F. Iacopi, Graphene growth on silicon carbide: A review, *Phys. Status Solidi A*, 2016, **213**, 2277–2289.

8 A. Pradeepkumar, N. Mishra, A. R. Kermany, J. J. Boeckl, J. Hellerstedt, M. S. Fuhrer and F. Iacopi, Catastrophic degradation of the interface of epitaxial silicon carbide on silicon at high temperatures, *Appl. Phys. Lett.*, 2016, **109**, 011604.

9 A. Pradeepkumar, M. Zielinski, M. Bosi, G. Verzellesi, D. K. Gaskill and F. Iacopi, Electrical leakage phenomenon

Open Access Article. Published on 19 2024. Downloaded on 11.05.26 11:41:40.
This article is licensed under a Creative Commons Attribution-NonCommercial 3.0 Unported Licence.

in heteroepitaxial cubic silicon carbide on silicon, *J. Appl. Phys.*, 2018, **123**, 215103.

10 A. Pradeepkumar, H. Cheng, K. Liu, M. Gebert, S. Bhattacharyya, M. Fuhrer and F. Iacopi, Low-leakage epitaxial graphene field-effect transistors on cubic silicon carbide on silicon, *J. Appl. Phys.*, 2023, **133**, 174503.

11 A. Pradeepkumar, D. K. Gaskill and F. Iacopi, Electronic and transport properties of epitaxial graphene on SiC and 3C-SiC/Si: a review, *Appl. Sci.*, 2020, **10**, 4350.

12 N. Mishra, J. J. Boeckl, A. Tadich, R. T. Jones, P. J. Pigram, M. Edmonds, M. S. Fuhrer, B. M. Nichols and F. Iacopi, Solid source growth of graphene with Ni–Cu catalysts: towards high quality *in situ* graphene on silicon, *J. Phys. D Appl. Phys.*, 2017, **50**, 095302.

13 F. Iacopi, N. Mishra, B. V. Cunning, D. Goding, S. Dimitrijev, R. Brock, R. H. Dauskardt, B. Wood and J. Boeckl, A catalytic alloy approach for graphene on epitaxial SiC on silicon wafers, *J. Mater. Res.*, 2015, **30**, 609.

14 A. Pradeepkumar, M. Amjadipour, N. Mishra, C. Liu, M. S. Fuhrer, A. Bendavid, F. Isa, M. Zielinski, H. Sirikumara, T. D. K. G. Jayasekera and F. Iacopi, p-type Epitaxial Graphene on Cubic Silicon Carbide on Silicon for Integrated Silicon Technologies, *ACS Appl. Nano Mater.*, 2019, 830–841.

15 B. V. Cunning, M. Ahmed, N. Mishra, A. R. Kermany, B. Wood and F. Iacopi, Graphitized silicon carbide microbeams: wafer-level, self-aligned graphene on silicon wafers, *Nanotechnol.*, 2014, **25**, 325301.

16 D. A. Katzmarek, A. Mancini, S. A. Maier and F. Iacopi, Direct synthesis of nanopatterned epitaxial graphene on silicon carbide, *Nanotechnol*, 2023, **34**, 405302.

17 M. Suemitsu and H. Fukidome, Epitaxial graphene on silicon substrates, *J. Phys. D Appl. Phys.*, 2010, **43**, 374012.

18 M. Jankowski, M. Saedi, F. La Porta, A. C. Manikas, C. Tsakonas, J. S. Cingolani, M. Andersen, M. de Voogd, G. J. van Baarle and K. Reuter, Real-time multiscale monitoring and tailoring of graphene growth on liquid copper, *ACS Nano*, 2021, **15**, 9638–9648.

19 S. Zheng, M. Zeng, H. Cao, T. Zhang, X. Gao, Y. Xiao and L. Fu, Insight into the rapid growth of graphene single crystals on liquid metal *via* chemical vapor deposition, *Sci. China Mater.*, 2019, **62**, 1087–1095.

20 M. Mauk, P. Sims, J. Rand and A. Barnett, in *Practical Handbook of Photovoltaics: Fundamentals and Applications*, ed. T. Markvart, Elsevier, USA, 2nd edn, 2012, ch. 4, pp. 161–206.

21 A. P. Le Brun, T.-Y. Huang, S. Pullen, A. R. Nelson, J. Spedding and S. A. Holt, Spatz: the time-of-flight neutron reflectometer with vertical sample geometry at the OPAL research reactor, *J. Appl. Crystallogr.*, 2023, **56**, 18–25.

22 Y. Ren and X. Zuo, Synchrotron X-ray and neutron diffraction, total scattering, and small-angle scattering techniques for rechargeable battery research, *Small Methods*, 2018, **2**, 1800064.

23 A. R. Nelson and S. W. Prescott, refnx: neutron and X-ray reflectometry analysis in Python, *J. Appl. Crystallogr.*, 2019, **52**, 193–200.

24 A. R. McCluskey, A. J. Caruana, C. J. Kinane, A. J. Armstrong, T. Arnold, J. F. Cooper, D. L. Cortie, A. V. Hughes, J.-F. Moulin and A. R. Nelson, Advice on describing Bayesian analysis of neutron and X-ray reflectometry, *J. Appl. Crystallogr.*, 2023, **56**, 12–17.

25 G. Pospelov, W. Van Herck, J. Burle, J. M. Carmona Loaiza, C. Durniak, J. M. Fisher, M. Ganeva, D. Yurov and J. Wuttke, BornAgain: software for simulating and fitting grazing-incidence small-angle scattering, *J. Appl. Crystallogr.*, 2020, **53**, 262–276.

26 P. Poulopoulos, A. Goschew, S. Pappas, V. Karoutsos, A. Straub, P. Fumagalli, M. Velgakis, W. Schommers and C. Politis, Graphene-Assisted Growth of Nanoblocks of Single-Crystalline Epitaxial Nickel Disilicides on Si (001), *J. Surf.*, 2014, **2**, 161–165.

27 A. M. Thron, P. K. Greene, K. Liu and K. van Benthem, Structural changes during the reaction of Ni thin films with (1 0 0) silicon substrates, *Acta Mater.*, 2012, **60**, 2668–2678.

28 G. W. C. Kaye and D. Ewen, The sublimation of metals at low pressures, *Proc. R. Soc. A*, 1913, **89**, 58–67.

29 E. Rollings, G.-H. Gweon, S. Zhou, B. Mun, J. McChesney, B. Hussain, A. Fedorov, P. First, W. De Heer and A. Lanzara, Synthesis and characterization of atomically thin graphite films on a silicon carbide substrate, *J. Phys. Chem. Solids*, 2006, **67**, 2172–2177.

30 C. Li, X. Li, W. Yu, R. Xiao, F. Huang, H. Tian, C. Wang, X. Chen and J. Shao, Scalable fabrication of turbostratic graphene with high density and high ion conductivity for compact capacitive energy storage, *Matter*, 2023, **6**, 4032–4049.

© 2024 The Author(s). Published by the Royal Society of Chemistry